Article

Fusion of Enhanced and Synthetic Vision System Images for Runway and Horizon Detection

Ahmed F. Fadhil[1], Raghuveer Kanneganti[2], Lalit Gupta[3] and Ravi Vaidyanathan[4*]

[1] Southern Illinois University; afadhil@siu.edu
[2] Southern Illinois University; r.kanneganti@siu.edu
[3] Southern Illinois University; lgupta@siu.edu
[4*] Correspondence: Imperial College London; r.vaidyanathan@ic.ac.uk; Tel.: +44-20-7594-7020

Abstract: UAV network operation enables gathering and fusion from disparate information sources for flight control in both manned and unmanned platforms. In this investigation, a novel procedure for detecting runways and horizons as well as enhancing surrounding terrain is introduced based on fusion of enhanced vision system (EVS) and synthetic vision system (SVS) images. EVS and SVS image fusion has yet to be implemented real-world situations due to signal misalignment. We address this through a registration step to align the EVS and SVS images. Four fusion rules combining discrete wavelet transform (DWT) sub-bands are formulated, implemented and evaluated. The resulting procedure is tested on real EVS-SVS image pairs and pairs containing simulated turbulence. Evaluations reveal that runways and horizons can be detected accurately even in poor visibility. Furthermore, it is demonstrated that different aspects of the EVS and SVS images can be emphasized by using different DWT fusion rules. The procedure is autonomous throughout landing, irrespective of weather. We believe the fusion architecture developed holds promise for incorporation into head-up displays (HUDs) and UAV remote displays to assist pilots landing aircraft in poor lighting and varying weather. The algorithm also provided a basis rule selection in other signal fusion applications.

Keywords: Unmanned Aircraft (UAV), Sensing, Intelligent transportation, Image fusion, Signal alignment, Runway detection, Image registration, Wavelet transform, Hough transform

1. Introduction

The precise detection of runways is crucial for safely landing aircraft; nearly half of aircraft accidents are reported to occur during the final approach and landing stages [1]. While instrumented landing systems have successfully been implemented to provide precise landing guidance, they are not available at all airports. Furthermore, smaller aircraft and fixed wing unmanned air vehicles (UAVs) often land in remote locations with only small runway strips available. Thus, there is a clear need to assist pilots and remote operators using visual flight landing aids to detect runways accurately in varying weather conditions. Readily available imaging systems offer obvious potential to address this issue, but a single mode of image capture often does not fully convey all vital landing information in time critical situations. Fusion of ground sensor arrays (e.g. infrared cameras [2]) have been proposed to provide real-time input to UAVs, in particular in the lack of GPS information [3]. Such systems can be enhanced with through the fusion of image information from disparate heterogeneous sensors in real-time.

The convolution of output acquired from multiple sensors capturing complementary information has received significant attention in recent years. Techniques for fusing such information from images have been applied to a diverse range of fields, including: medical imaging [4, 5], remote sensing [6,7], intelligent transport [8,9], surveillance [10], low altitude remote sensing [11], and color visibility enhancement [12]. Very recent approaches [13] have introduced weighted

Preprints (www.preprints.org) | NOT PEER-REVIEWED | Posted: 16 October 2018 doi:10.20944/preprints201810.0343.v1

fusion strategies aimed at improving the robustness of detection robustness against the size of object. Such approaches hold intriguing potential for detection of weakly illuminated areas, which provide particular challenges in recognition which have not been fully addressed today [14]. Fusion of images with complementary vehicle control information have been also been introduced for UAVs [15] as well as algorithms combining infrared and visible spectrum images for target tracking [16].

The accurate detection of runways has conversely received considerable attention in the literature. A variety of techniques have been developed to detect runways in aerial images using the Hough transform and least squares to obtain boundary information [17], registering the runway with known reference images in different orientations [18], edge detection in conjunction with Hough transform line detection [19], and intensity and contrast of the runway and background [20]. Runways have also been detected in satellite images using texture properties [21], edge detection in conjunction with the Hough transform and chain codes [22], Helmholtz principle [23], shape and chroma features [24], as well as edge detection and fuzzy logic [25]. Detecting runways is also an important part of obstacle detection on runways [26]–[28]. Related efforts have also focused on horizon detection in low visibility conditions [26] and to identify the ground in images for emergency landings [30].

While image fusion represents an obvious approach for runway detection, Liu and Yu [31] argued that the majority of approaches today still rely on the assumption that source images are perfectly aligned. This is not the case in many practical field applications of image processing. The runway and horizon detection and enhancement approach introduced in this paper is based on exploiting information from enhanced vision system (EVS) and synthetic vision system (SVS) images of the runways. Therefore these images for aircraft runway detection and enhanced situational awareness first need to be aligned to fully capture their complementary image information.

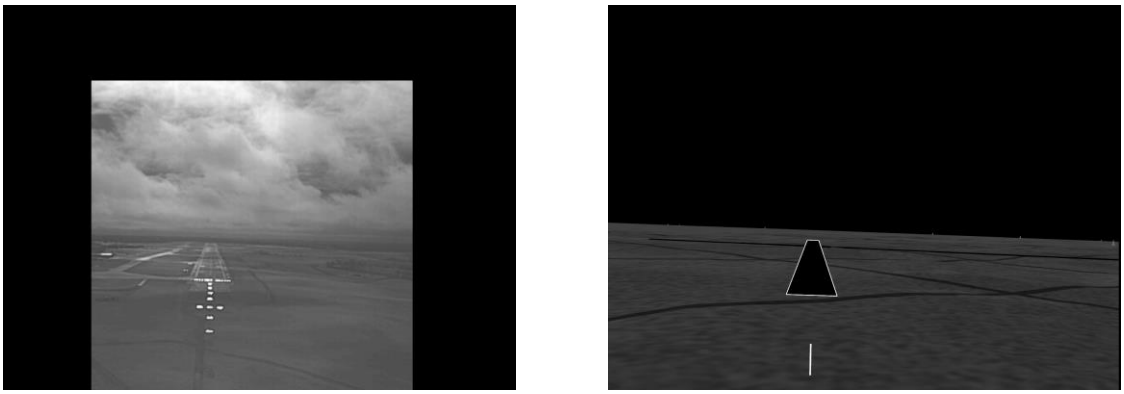

(a) (b)

Figure 1: An example of (a) EVS and (b) SVS image frames.

Figure 1 shows examples of EVS and SVS images of a runway. The EVS image is an infra-red image of the runway and the SVS image is a GPS generated image of the runway. The EVS image can be used by pilots during landing but the quality of the EVS image is affected by adverse weather conditions. Unlike the EVS image, the SVS image is not affected by the weather. However, the SVS image is not a "real" image of the runway and cannot be used solely to help the pilot safely land the aircraft. The approach developed in this paper is to exploit the weather-invariant SVS image information to accurately detect the runway in the weather-dependent EVS image and to generate an EVS-SVS composite image which contains information from both images. The EVS and SVS images are not aligned, therefore first the images are registered using runway and horizon features

Preprints (www.preprints.org) | NOT PEER-REVIEWED | Posted: 16 October 2018 doi:10.20944/preprints201810.0343.v1

prior to fusion. Different fusion rules are developed to combine the EVS and SVS images and evaluated in the presence of varying levels of atmospheric turbulence.

The principal research objective is to create image frames that contain enhanced runway and surrounding information by fusing the EVS and SVS images so they can be incorporated into head-up displays (HUDs) or unmanned aerial vehicle (UAV) remote displays to assist pilots in safely landing aircrafts. The objective requires both accurately detecting the runway in a sequence of frames through registration and then enhance the information surrounding the runway by fusing the EVS and SVS images. Information from the weather-independent SVS image are used to approximate the runway and horizon in the weather-dependent EVS image. The SVS image is aligned and fused with the EVS image. The most critical need for accurate runway detection is during the landing phase, therefore the focus is on registering and fusing the EVS and SVS images when the aircraft is close to the runway. The procedure is made autonomous from frame-to-frame by deriving parameters from the SVS image. The performance of the fusion methodology is validated on a data set consisting of 1350 pairs of EVS and SVS frames of the runway acquired while an aircraft was landing. Furthermore, additional subjective and objective evaluations are conducted using simulated EVS images with varying levels of atmospheric turbulence.

Related work includes noteworthy studies that focus on using synthetic vision data to accurately locate the position of the runway and then detect moving objects on the runway [28], fusing real and virtual information to enhance airport scenes [32], and integrating EVS and SVS data to improve visibility in adverse atmospheric conditions [33]. The work described in this paper differs from these, because the primary focus is on both runway and horizon detection as well as the fusion of EVS and SVS images to provide improved visual information of the runway scene. The formulations of the steps to detect runways and horizons, to fuse images, and to evaluate the performance subjectively represent the principal contributions of this work..

2. EVS and SVS Image Registration

In general, image registration is the geometrical alignment of two or more images of the same scene it can be particularly challenging when images may exist in different feature spaces [34]. Image registration algorithms can be classified into two groups: feature-based registration and area-based registration [35]. The feature-based registration method is employed in this study. Because the goal of this study is to fuse the runways as well as the surrounding areas, features for registration are derived from the runways and the horizons. The features selected for registration are the runway corners and the horizon end-points. It is assumed that the runway is a quadrilateral and the horizon is a long straight-line segment in both the EVS and SVS images. The runway quadrilateral is composed of two long line segments and two shorter line segments. The runway corners can, therefore, be determined by detecting the end-points of the two long line segments. The horizon end-points can be determined from the line segment corresponding to the horizon. The first step, therefore, is to detect line segments in the EVS and SVS images and select those line segments that correspond to the two longer runway segments and the horizon line. The ith EVS and SVS frames are represented by $f_{E_i}(x,y)$ and $f_{S_i}(x,y)$, respectively. Because the SVS image quality is good and is unaffected by the weather conditions, the runway and horizon are first detected in the SVS image. The SVS runway and horizon information are used to estimate the runway and horizon in the corresponding EVS image. Because similar operations are performed on successive frames, the formulations of the steps to register and fuse the SVS and EVS frames are simplified by dropping the subscript i.

2.1 SVS Runway and Horizon detection

A careful examination of the SVS image frames reveal that the following useful information (i) the image is a simple gray-scale image, (ii) the runway is outlined by a bright boundary, and (iii) the

Preprints (www.preprints.org) | NOT PEER-REVIEWED | Posted: 16 October 2018 doi:10.20944/preprints201810.0343.v1

horizon is a distinct boundary between the all-dark sky and the brighter non-sky regions. In the first step, the runway is detected by segmenting $f_S(x,y)$ according to:

$$g_S(x,y) = \begin{cases} 1, & if\, f_S(x,y) > (\delta_S) Max[f_S(x,y)] \\ 0, & otherwise \end{cases} \quad (1)$$

The factor $\delta_S, 0 < \delta_S < 1,$ is determined empirically so that the resulting binary image $g_S(x,y)$ contains only the bright runway border. The four corner points of the runway are selected as runway registration control points in the SVS image. The end-points of the horizon, which will serve as horizon registration control points, are found by detecting the transition point from the dark pixels to the brighter pixels in the first and last columns of the image. The line joining the end-points defines the horizon in the SVS image. Figure 2(a) shows, in blue, the runway and horizon extracted from the SVS image in Figure 1 using $\delta_S = 0.5$ which was found to give good segmentation results across all 1350 SVS frames. If $g_S(x,y)$ is the binary image of the runway and horizon, the angles of the two long runway line segments and the horizon line can be found from the co-linearity Hough transform $\{S(\rho,\theta)\}$ of $g_S(x,y)$. Let $\{S(\rho,\theta_1)\}$ be the Hough transform accumulator cell with the highest count and let $\{S(\rho,\theta_2)\}$, and $\{S(\rho,\theta_3)\}$ be the cells with the next two highest counts. Then, the horizon angle is given by θ_1 and the runway angles are given by θ_2 and θ_3. The angle parameters will be used to determine the runway lines and horizon in the EVS image. Additionally, the area A_s, of the runway quadrilateral is determined. As noted in the introduction, the focus is on registering and fusing the EVS and SVS images only when the aircraft is approaching the runway. The runway area is used as a parameter to indicate when the registration and fusion should begin. To make this parameter dimensionless, the parameter is normalized by dividing it by the frame area A, that is, (A_s/A). Registration begins when the area ratio exceeds a threshold λ. This step may seem unnecessary, however, there is clearly no need to register the images when the aircraft is far from the runway.

2.2 EVS Runway and Horizon Detection

Unlike the SVS image, the EVS image can be relatively complex. Consequently, the runway cannot be determined directly through segmentation. Nor can the horizon be detected using the method developed for the SVS image. Moreover, the EVS frames are bound to be degraded with noise. In order to decrease the effects of noise, the EVS frames are filtered using a Weiner filter [36]. In the frequency domain, the EVS filtered image is given by

$$\hat{F}_E(u,v) = \left[\frac{1}{H(u,v)} \frac{|H(u,v)|^2}{|H(u,v)|^2 + K}\right] F_E(u,v) \quad (2)$$

where $H(u,v)$ is the degradation function, $F_E(u,v)$ is the Fourier transform of $f_E(x,y)$, and K is a specified constant. The main degradation is assumed to be atmospheric turbulence, therefore, the function:

$$H(u,v) = e^{-k(u^2+v^2)^{5/6}} \quad (3)$$

which is often used to model turbulence [36], is selected. The constant k can be adjusted according to the amount of turbulence.

The runway and horizon in the EVS image $\hat{f}_E(x,y)$ are detected using information extracted from the SVS image. The SVS runway and horizon serve as initial approximations for the EVS

Preprints (www.preprints.org) | NOT PEER-REVIEWED | Posted: 16 October 2018 doi:10.20944/preprints201810.0343.v1

runway and horizon, respectively. In order to detect the runway in the EVS image, let $\hat{r_E}(x,y)$ be a rectangular region encompassing the approximated runway. The two long runway sides are within the diagonal and vertical orientations when the aircraft approaches the runway. Therefore, $\hat{r_E}(x,y)$ is converted into a region $r_E(x,y)$ containing vertical and approximately vertical lines by applying a (3×3) vertical line detection mask [36]. The region $r_E(x,y)$ is converted into a binary region $g_E(x,y)$ using the following segmentation rule:

$$g_E(x,y) = \begin{cases} 1, & if \hat{r_E}(x,y) > (\delta_E) Max[\hat{r_E}(x,y)] \\ 0, & otherwise \end{cases} \quad (4)$$

where, δ_E is determined empirically so that the resulting binary image contains only the bright line segments and removes the lower-intensity line segments. The Hough transform $\{E(\rho,\theta)\}$ of $g_E(x,y)$ is computed and the pixels contributing to accumulator cells $\{E(\rho,\theta_2 \pm \alpha)\}$ and $\{E(\rho,\theta_3 \pm \alpha)\}$ are selected to determine line segments that have approximately the same orientations as the SVS runway. The two largest line segments satisfying $\{E(\rho,\theta_2 \pm \alpha)\}$ and $\{E(\rho,\theta_3 \pm \alpha)\}$ are selected as the runway line segments in the EVS image. The parameter α is included to account for the fact that runway is not perfectly aligned in the SVS and EVS images. The end-points of these two line segments give the runway registration control points in the EVS image. Moreover, the lines connecting the runway control points define the estimated runway in the EVS image. The estimated runway, which tends to compactly enclose the actual runway, is superimposed onto the EVS image using an intensity equal to 255. In a similar manner, the horizon in the EVS image is estimated by using the SVS horizon as an initial approximation and finding the dominant line within $(\theta_1 \pm \alpha_1)$ from the Hough transform in a band encompassing the initial approximation. The two-end points of the horizon give the horizon control points in the EVS image. The line joining the two end-points is superimposed on the EVs image using an intensity equal to 255. Figure 2(b) shows the estimated runway and horizon in the EVS image of Figure 1 using the following values for the parameters: $k = 0.0025$, $\delta_E = 0.6$, $\alpha = 30°$, $\alpha_1 = 25°$. These values were found to give good results across the last 350 EVS frames that were involved in registration.

(a) (b)

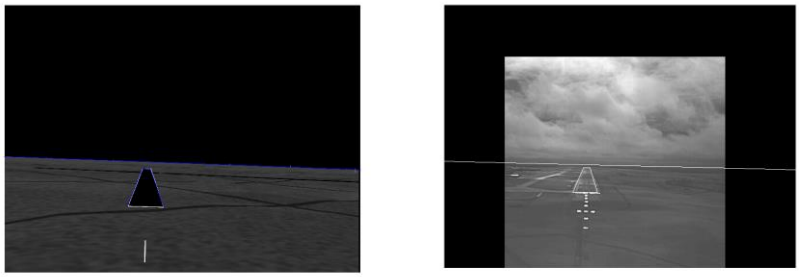

Figure 1: The runway and horizon detected in the (a) SVS image (b) EVS image.

The horizon is assumed to be a straight line in the above formulations because the horizons in the data set used in this study are straight lines. Moreover, it is not unusual to make this assumption [29; 30]. The formulation can, however, be modified for the more general case in which the horizon is not a straight line. For example, the pixels forming the SVS horizon can be found by detecting the transition points from the dark pixels to the brighter pixels in all columns of the SVS image. This horizon will serve as the initial approximation in the EVS image. The EVS horizon can then be determined in a band containing the initial approximation by detecting the sky-to-land transitions in each column of the EVS image.

Preprints (www.preprints.org) | NOT PEER-REVIEWED | Posted: 16 October 2018 doi:10.20944/preprints201810.0343.v1

2.3 Jitter Detection and Correction

The detection of the runway corners in the EVS image depends on its quality. Frame-to-frame changes can vary the detected corner locations significantly resulting in "jitter" in the detected runway across successive frames. This jitter is clearly undesirable because the detected runway should not "bounce around" while the aircraft is landing. In order to avoid runway jitter, the corners of the previous frame are used to determine if the corners in the current frame will lead to jitter. If $d_i$is the distance between each pair of corner points (x_i, y_i) and (x_{i-1}, y_{i-1}) in the current and previous frames, respectively, and A_E is the area of the runway in the EVS image, the normalized distance (d_i/A_E) in the current and previous frame is compared with a threshold ρ. If (d_i/A_E) exceeds the threshold ρ, the corner point in the current frame is replaced with the corner point in the previous frame to prevent jitter. The median of the five previous corner points is used to update the previous frame corner points to insure accuracy even when the corners in the previous frames are indistinct.

2.4 Horizon and Runway Registration

Although not obvious visually, the runways and horizons in the SVS and EVS images are not aligned in Figures 2(a) and 2(b). This is demonstrated in Figure 3(a) which shows the result of superimposing the SVS runway and horizon of Figure 2(a) onto Figure 2(b). Clearly, the two images have be registered prior to fusion. A two-step registration procedure is developed in which the two images are first globally aligned based on horizon registration and then locally aligning the runways in the horizon-aligned images. Because the key information for landing is in the real EVS image, the SVS image is registered to the EVS image. That is, the SVS image is the target image and the EVS image is the reference image. The horizon corner points, top image corner points, and the bottom image corner points are the six pairs of control points selected for the horizon based registration. The runway corner points and the corner points of the runway encompassing rectangle $r(x, y)$ are selected as the control points for registering the runways. The rectangle $r(x, y)$ covers exactly the same regions in both images and is the also the same as region $r_E^A(x, y)$ used to encompass the initial runway approximation in the EVS image. For both steps, the projective transformation is applied to register the images and the results of registering the images in Figure 2(a) and 2(b) are shown in Figure 3(b). Note that the blue and white lines are perfectly aligned and almost appear as single blue lines. Additional registration examples will be presented in conjunction with the SVS and EVS fusion results.

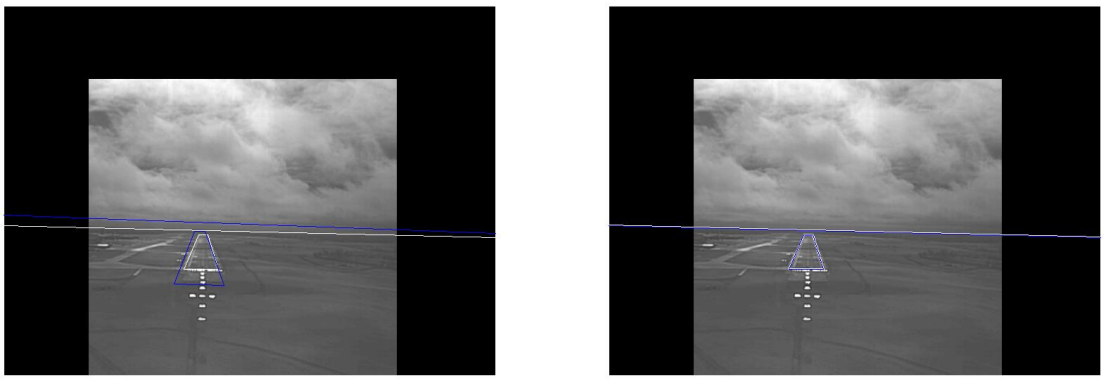

(a) (b)

Figure 2: Superimposed SVS horizon and runway onto the EVS image with (a) no registration (b) with registration.

Preprints (www.preprints.org) | NOT PEER-REVIEWED | Posted: 16 October 2018 doi:10.20944/preprints201810.0343.v1

2.5 Absence of Runway Approach-Line in the EVS and SVS Images

Typically, the runway approach-line (the bottom line of the runway) is not visible in the SVS ad EVS images when the aircraft is about to land on the runway as shown in Figure 4. This case is automatically detected when two corner points fall in the last row of the SVS image. At this stage of landing, the primary focus is on aligning and fusing the runways in the SVS and EVS images. The runway has a center line which pilots use to align the aircraft. This line is approximately vertical and can be determined from the Hough transform of the EVS image. A center line is generated in the SVS runway by connecting the midpoints of top and bottom corner points. The images are registered by aligning the pair of center lines. Examples will be shown in the experiments section.

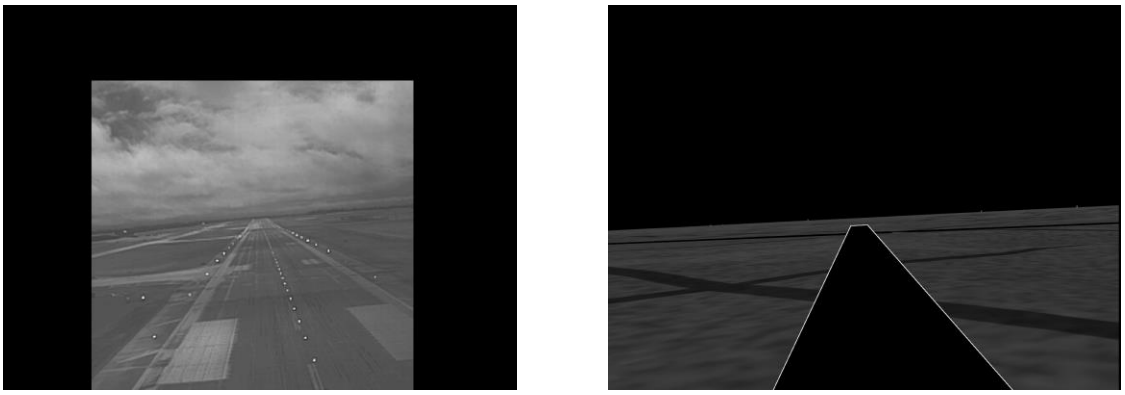

(a) (b)

Figure 3: Frames which do not contain the runway approach-line (a) EVS frame (b) SVS frame.

3. EVS and SVS Image Fusion

Image fusion is the process of combining two or more images in such a way that information from both images is preserved [38]. The goal here is to generate an image $w_{ES}(x,y)$ which is obtained by fusing the Weiner filtered EVS image $w_E(x,y)$ and the registered SVS image $w_S(x,y)$. The fused image is given by

$$w_{ES}(x,y) = w_E(x,y) \blacksquare w_S(x,y) \quad (5)$$

where $\blacksquare$ represents the fusion rule. Different aspects of the two images can be displayed in a single image by applying different fusion rules. The images can be fused directly in the spatial domain [38] or in a transform domain such as the wavelet domain [37]. Although quite simple, the spatial domain rules are limited to the global application of operations such as pixel averaging or maximum selection [39], [40]. Conversely, the wavelet domain rules offer greater flexibility in developing fusion rules. For example, different fusion rules can be applied to combine the wavelet sub-bands [38-43]. This flexibility is the primary reason for selecting and developing fusion rules based on the DWT in this study. In most fusion applications, equal weightage is given to both images in the sense that fused image should capture the information from both images equally. Consequently, the correlation between the fused image and the two original images is often used as a measure to evaluate the fusion performance [40; 41; 44]. In this study, however, equal weightage is not assumed because the EVS image is more important than the "supplementary" information in the SVS image. If the dimension of $w_E(x,y)$ is assumed to be $M \times N$, the DWT of $w_E(x,y)$ can be written as

$$W_E^a(m,n) = \frac{1}{\sqrt{MN}} \sum_{x=0}^{M-1} \sum_{y=0}^{N-1} w_E(x,y)\, \varphi_{m,n}(x,y) \quad (6)$$

$$W_E^i(m,n) = \frac{1}{\sqrt{MN}} \sum_{x=0}^{M-1} \sum_{y=0}^{N-1} w_E(x,y)\, \psi^i{}_{m,n}(x,y), i = \{h,v,d\} \quad (7)$$

Preprints (www.preprints.org) | NOT PEER-REVIEWED | Posted: 16 October 2018 doi:10.20944/preprints201810.0343.v1

where the scaled and translated basis functions are given by:

$$\varphi_{m,n}(x,y) = 2^{j/2}(x,y)\varphi\left(2^j x - m, 2^j y - n\right) \quad (8)$$

$$\psi^i{}_{m,n}(x,y) = 2^{j/2}\psi^i(2^j x - m, 2^j y - n), i = \{h,v,d\} \quad (9)$$

The basis functions are assumed to be separable and can, therefore, be written as

$$\varphi_{m,n}(x,y) = \varphi(x)\varphi(y) \quad (10)$$

$$\psi^i{}_{m,n}(x,y) = \psi(x)\psi(y), i = \{h,v,d\} \quad (11)$$

In a notable study, extensive experiments have shown that different basis functions tend to give similar fusion results [42]. The Haar wavelet transform is selected in this study because of its computational simplicity. For the Haar transform, the 1-dimensional scaling and wavelet vectors are given by:

$$\varphi(x) = \begin{cases} \frac{1}{\sqrt{2}} x = 0,1 \\ 0 \quad otherwise \end{cases} \quad (12)$$

$$\psi(x) = \begin{cases} \frac{1}{\sqrt{2}} x = 0 \\ \frac{-1}{\sqrt{2}} x = 1 \\ 0 \quad otherwise \end{cases} \quad (13)$$

The corresponding inverse wavelet transform is then given by:

$$w_E(x,y) = \frac{1}{\sqrt{MN}}\left[\sum_{m=0}^{\frac{M}{2}-1}\sum_{n=0}^{\frac{N}{2}-1} W_E^a(m,n)\,\varphi_{m,n}(x,y) + \sum_{i=h,v,d}\sum_{m=0}^{\frac{M}{2}-1}\sum_{n=0}^{\frac{N}{2}-1} W_E^i(m,n)\psi^i{}_{m,n}(x,y)\right] \quad (14)$$

where $W_E^a(m,n)$, $W_E^v(m,n)$, $W_E^h(m,n)$, and $W_E^d(m,n)$ are the four $(M/2)\times(N/2)$ sub-bands of the DWT of $w_E(x,y)$. These sub-bands are the approximation, vertical detail, horizontal detail, and diagonal detail sub-bands of $w_E(x,y)$. Similarly, $W_S^a(m,n)$, $W_S^v(m,n)$, $W_S^h(m,n)$, and $W_S^d(m,n)$ represent the sub-bands of the DWT of $w(x,y)$. Using the DWT sub-bands the images can be fused according to the following rules:

Maximum Selection Rule

$$W_{ES}^a(m,n) = MAX[W_E^a(m,n), W_S^a(m,n)] \quad (15)$$

$$W_{ES}^v(m,n) = MAX[W_E^v(m,n), W_S^v(m,n)]$$

$$W_{ES}^h(m,n) = MAX[W_E^h(m,n), W_S^h(m,n)]$$

$$W_{ES}^d(m,n) = MAX[W_E^d(m,n), W_S^d(m,n)]$$

Average Selection Rule

$$W_{ES}^a(m,n) = AVG[W_E^a(m,n), W_S^a(m,n)] \quad (16)$$

$$W_{ES}^v(m,n) = AVG[W_E^v(m,n), W_S^v(m,n)]$$

$$W_{ES}^h(m,n) = AVG[W_E^h(m,n), W_S^h(m,n)]$$

$$W_{ES}^d(m,n) = AVG[W_E^d(m,n), W_S^d(m,n)]$$

Mixed Selection Rule

$$W_{ES}^a(m,n) = AVG[W_E^a(m,n), W_S^a(m,n)] \quad (17)$$

$$W_{ES}^v(m,n) = MAX[W_E^v(m,n), W_S^v(m,n)]$$

$$W_{ES}^h(m,n) = MAX[W_E^h(m,n), W_S^h(m,n)]$$

$$W_{ES}^d(m,n) = MAX[W_E^d(m,n), W_S^d(m,n)]$$

Modified Selection Rule

Preprints (www.preprints.org) | NOT PEER-REVIEWED | Posted: 16 October 2018 doi:10.20944/preprints201810.0343.v1

$$W_{ES}^{a}(m,n) = W_{E}^{a}(m,n) \quad (18)$$

$$W_{ES}^{v}(m,n) = MAX[W_{E}^{v}(m,n), W_{S}^{v}(m,n)]$$

$$W_{ES}^{h}(m,n) = MAX[W_{E}^{h}(m,n), W_{S}^{h}(m,n)]$$

$$W_{ES}^{d}(m,n) = MAX[W_{E}^{d}(m,n), W_{S}^{d}(m,n)]$$

where, $W_{ES}^{a}(m,n)$, $W_{ES}^{v}(m,n)$, $W_{ES}^{h}(m,n)$, and $W_{ES}^{d}(m,n)$ are the sub-bands of the EVS-SVS fused image. The fused image $w_{ES}(x,y)$ is obtained from the inverse wavelet transform after application of the selection rule. Note that most often, images are fused using the maximum, average, or mixed rules [38-43]. The modified rule is introduced to give more weight to the EVS image by preserving the EVS information in the approximation band and can be regarded as a modification of the maximum and mixed rules. All four fusion rules are implemented and evaluated in the next section.

4. Registration and Fusion Experimental Results

This section describes the experiments designed to evaluate the overall procedure developed to register and fuse the EVS and SVS image frames. The data set, provided by Rockwell-Collins, consists of 1350 EVS and SVS image pairs acquired from the infra-red sensor on an aircraft and a satellite, respectively. The dimensions of EVS and SVS frames are 1050×1400 and the frame rate was 6 fps. The following values were used for the parameters: $\delta_S = 0.5$, $\lambda = 0.00885$, $k = 0.0025$, $K = 10^{-8}$, $\delta_E = 0.6$, $\alpha = 30°$, $\alpha_1 = 25°$, $\rho = 10^{-5}$. After setting the parameters, the entire sequence of frame pairs were processed autonomously without any intervention.

Clearly, it is not practical to show the results for all 1350 frame pairs, therefore, only a few select examples which show different stages of approach and landing are shown to conduct subjective evaluations. Also, the real data set does not cover varying weather conditions. In order to conduct more detailed subjective and objective evaluations, data sets containing various levels of atmospheric turbulence in the EVS frames are generated using the same degradation model $H(u,v)$ used to filter the EVS image. Two sets of EVS frames were generated to simulate intermediate level turbulence using k=0.001, and severe level turbulence using k=0.0025 in each frame. Examples of degraded EVS frames are shown in Figure 5. The registration performance can thus be evaluated objectively by the root-mean-square (rms) error between the manually detected runway corner points and horizon points in the EVS image, selected using mouse-clicks, and the corner points detected by the registration procedure.

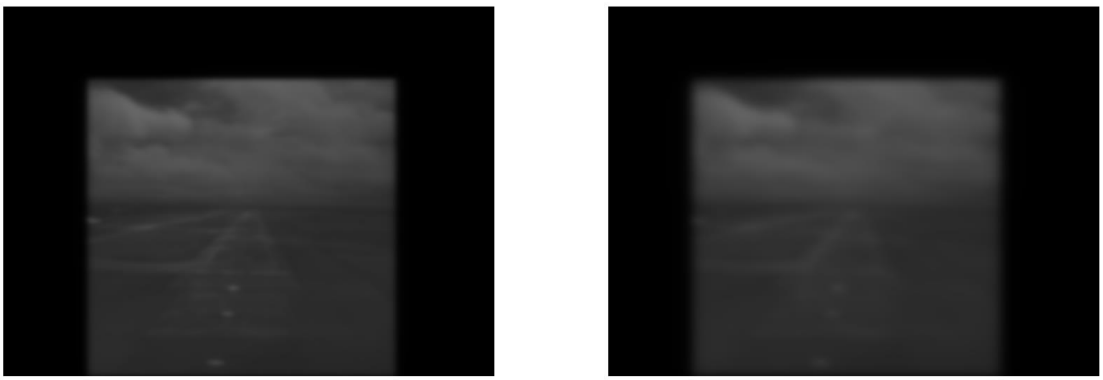

(a) (b)

Figure 4: (a) EVS image with intermediate turbulence (b) EVS images with severe turbulence.

Preprints (www.preprints.org) | NOT PEER-REVIEWED | Posted: 16 October 2018 doi:10.20944/preprints201810.0343.v1

Figure 6 shows examples of fusing the EVS and SVS images directly using the maximum fusion rule without prior registration. The runways, horizons, and center lines in the SVS and EVS images are shown in blue and red, respectively, to facilitate visual analysis. Observe the following problems: (i) the runways and horizons are not aligned in Figure 6(a), (ii) the horizons and runway center lines are not aligned in Figure 6(b) and (iii) the SVS runway is much larger than the EVS runway in Figure 6(a). Similar problems are observed with the four other fusion rules. Figure 7 shows the fusion results of the same images after they have been registered. Observe that the runways, center lines, and horizons are aligned quite well.

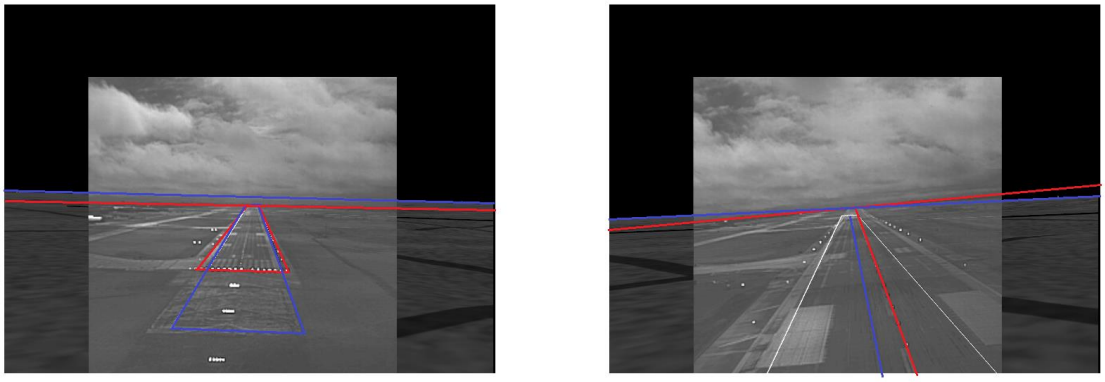

Figure 5: Examples EVS-SVS image fusion without prior registration.

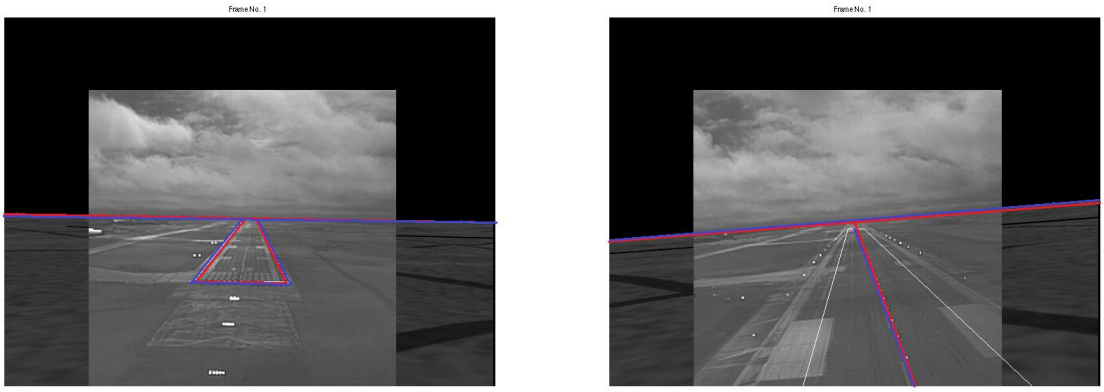

Figure 6: Examples of EVS-SVS image fusion with registration.

4. Discussion

Examples of fusing pairs of registered EVS and SVS images using the four fusion rules are shown in Figures 8 and 9 for the original (no-turbulence assumption) and severe turbulence cases, respectively. The most important results are for the severe turbulence case because there is not much need for runway and horizon detection when there is little or no atmospheric turbulence. The no-turbulence results are included to draw general conclusion relating to the characteristics of the images combined by using different fusion rules. It is interesting to observe the following characteristics in the results:

(a) The results for the no-turbulence case show subtle but expected differences amongst the four rules. The maximum selection rule tends to favor the brighter image in the approximation band which is typically the EVS image. Selecting the maximum in the other sub-bands tends to sharpen the edges in the fused image. Consequently, as evident in Figure 8(a), the runway and horizon appear brighter in the fused image. The average selection rule preserves details

Preprints (www.preprints.org) | NOT PEER-REVIEWED | Posted: 16 October 2018 doi:10.20944/preprints201810.0343.v1

from both images with equal weighting. However, there is a slight loss in contrast throughout the fused image due to smoothing which is typical of averaging. Moreover, averaging the approximation bands, which are low frequency bands, will tend to blur the low frequencies which is undesirable. A careful examination of Figure 8(b) confirms this loss in contrast in the entire image. The mixed selection rule preserves the EVS and SVS approximation details with equal weighting while sharpening the high frequencies. As a result, the fused image in Figure 8(c) appears to be sharper, however, there is a slight loss in the contrast due to averaging the approximation sub-bands. The modified selection rule preserves the EVS approximation information completely while enhancing the high frequency information. Consequently, the fused image in Figure 8(d) is sharper and looks similar to the maximum rule which favors the brighter EVS image.

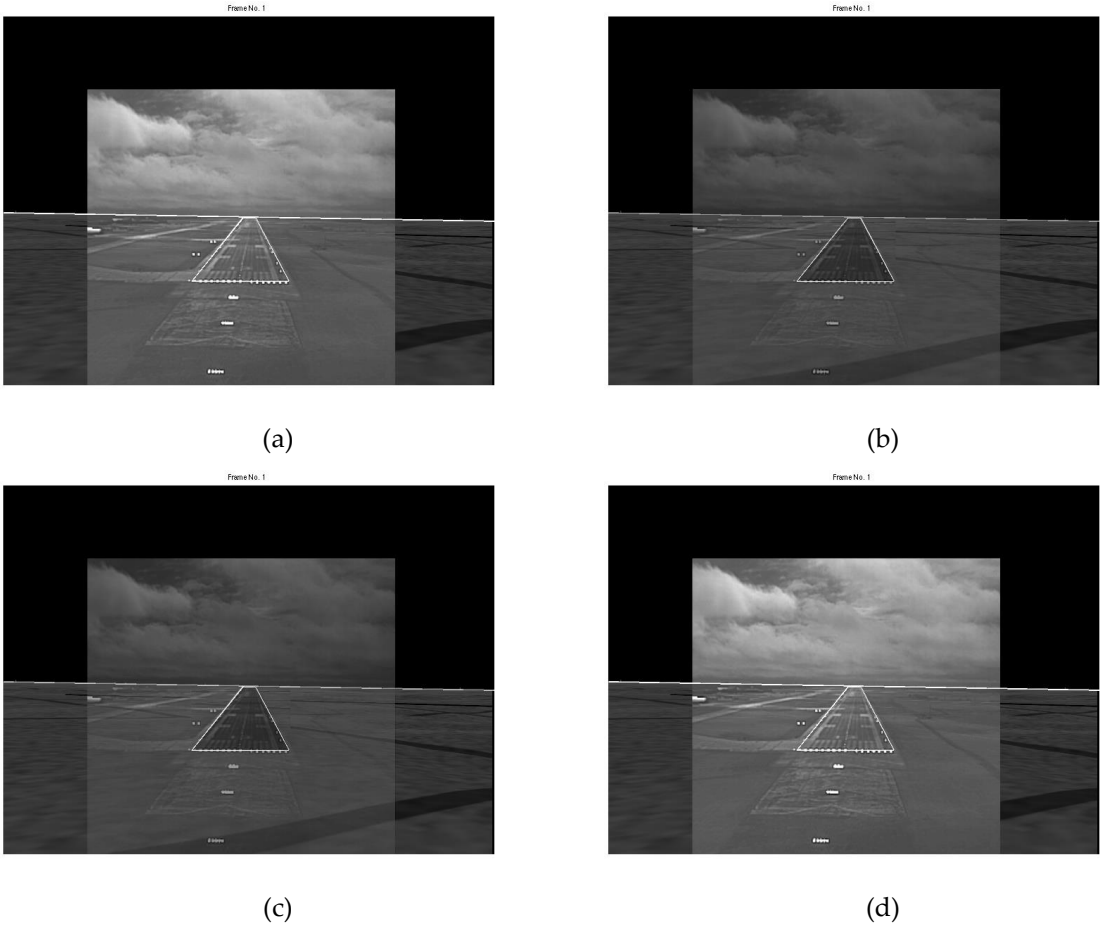

(a) (b)

(c) (d)

Figure 7: Fusion in no-turbulence (a) Maximum rule (b) Average rule (c) Mixed rule (d) Modified rule.

(b) The general characteristics observed for the no-turbulence case also hold for the severe turbulence case, however, there are some important differences across the four fusion results shown in Figure 9. For example, the maximum rule tends to preserve more of the SVS information, as seen in Figure 9(a) because the SVS image is brighter than the EVS image. This is quite undesirable. The results for the average and mixed rules shown in Figure 9(b) and 9(c), respectively, are also quite unsatisfactory because of the overall decrease in contrast. The best result, shown in Figure 9(d), is obtained using the modified rule because it preserves the important EVS information while also fusing the lesser important SVS information. Most importantly, the runway details are the clearest in Figure 9(d) which can also be useful for detecting obstacles on runways.

Preprints (www.preprints.org) | NOT PEER-REVIEWED | Posted: 16 October 2018 doi:10.20944/preprints201810.0343.v1

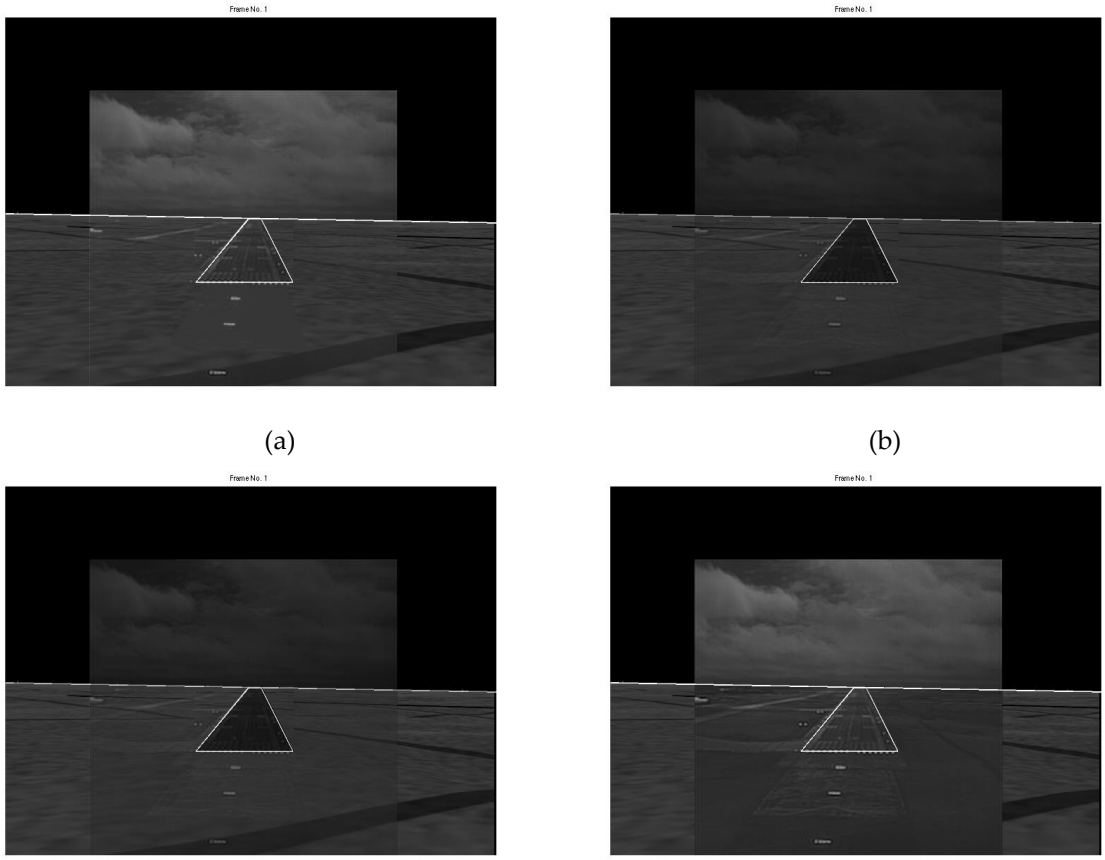

(a) (b)

(c) (d)

Figure 8: Fusion in severe turbulence (a) Maximum rule (b) Average rule (c) Mixed rule (d) Modified rule.

Although the differences in the fused images are subtle, the observed characteristics can be used as a guide for selecting fusion rules based on what aspects of the two images need to be emphasized in various applications. The next set of results are included to evaluate the registration performance by evaluating the rms distance error between the locations of the manually detected runway and horizon corners points and locations of the registered runway and horizon corner points. Figure 10 summarizes the rms errors obtained from the original data set without registration, the original data set with registration, and the two simulated degraded data sets with registration. The results cover frames 1101 to 1190. The frames are ordered such that the frame number increases as the distance between the aircraft and runway decreases. The original data set without registration is included to compare the registration performance.

(a) (b)

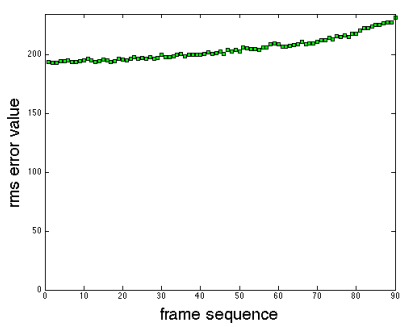

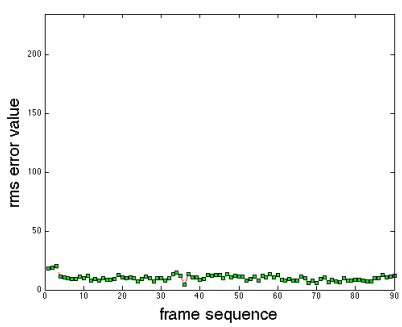

Preprints (www.preprints.org) | NOT PEER-REVIEWED | Posted: 16 October 2018 doi:10.20944/preprints201810.0343.v1

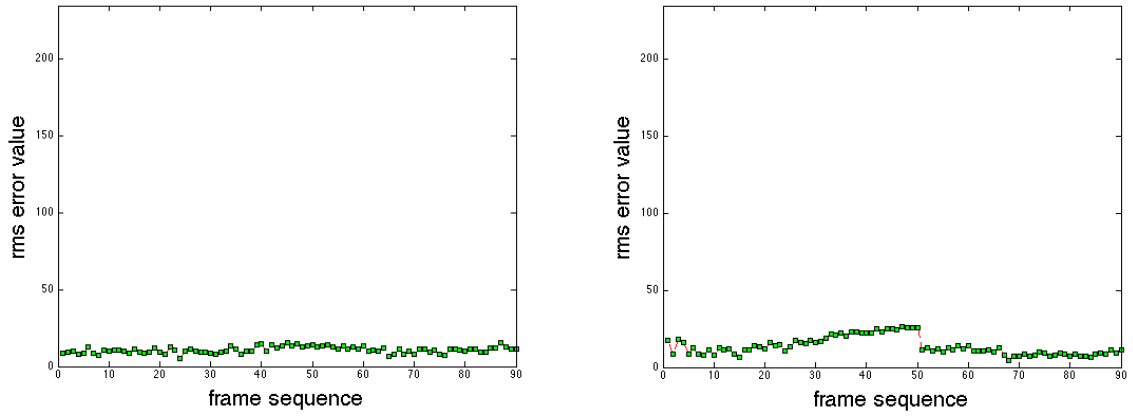

Figure 9: Corner and horizon registration rms errors (a) original data set with no registration (b) original data set with registration (c) data set with intermediate turbulence (d) data set with severe turbulence.

The following points should be noted regarding the results presented in Figure 10:

(a) When no registration is employed, the rms errors are relatively high. Moreover, the rms errors increase when the distance between the aircraft and the runway decreases. This increase is clearly undesirable because it is even more critical to detect the runway accurately as the aircraft gets closer to the runway.

(b) The rms errors are smaller when registration is employed. Most importantly, the errors do not increase when the aircraft gets closer to the runway.

(c) The error trends across the registered results are quite similar. Furthermore, the increase in the rms errors in the presence of severe turbulence is marginal.

(d) The various parameters were exactly the same for the four sets of results. No attempt was made to adjust the parameters to accommodate the different levels of turbulence in Figures 10(c) and 10(d).

(e) Although it is not possible to show in this paper, the jitter is observed to be minimal when the registered and fused frames are displayed as a video at the frame capture rate.

5. Conclusions

An innovative procedure has been introduced to accurately detect runways and horizons as well as enhance surrounding runway areas by fusing EVS and SVS images. Central to the procedure is a novel fusion method for EVS and SVS runway images captured from an aircraft in the final stages of landing. A registration algorithm is further introduced to align the EVS and SVS images prior to fusion. The most notable feature of the registration is its guidance is based solely on information extracted from weather-invariant SVS images. Four fusion rules based on combining DWT sub-bands have been implemented, contrasted, and evaluated. The resulting procedure has been tested on real EVS-SVS image pairs and also on image pairs containing simulated EVS images with varying levels of turbulence. The subjective and objective evaluations reveal that runways can be detected accurately, even in poor visibility conditions due to severe levels of atmospheric turbulence. It has also been demonstrated that different aspects of the EVS and SVS images can be emphasized by use of different DWT-based fusion procedures. The modified rule was judged to yield the best fusion results for the problem under consideration. Another notable feature is that the entire procedure is autonomous throughout the landing sequence, irrespective of the weather conditions; the fixed parameters are set initially and variable parameters are determined automatically from image frames during operation. Given the excellent fusion results and the autonomous feature, it can be concluded that the fusion procedure developed holds strong potential

for incorporation into head-up displays (HUDs) to assist pilots in safely landing aircrafts in varying weather conditions. The system can also be implemented to help remotely piloted UAVs landing in challenging conditions in remote locations. Furthermore, the procedure developed can be easily modified to fuse image pairs in different applications. The observations and results can also serve as a guide for selecting different fusion rules for a given application.

Author Contributions:

Ahmed F. Fadhil contributed to programming, testing, validation and data analysis.
Raghuveer Kanneganti contributed programming, experimental data analysis, and validation.
Lalit Gupta was responsible for algorithm development, methodology, project administration, funding acquisition, writing, and formal analysis.
Ravi Vaidyanathan contributed to conceptualization, formal analysis, investigation, writing, review and editing, and funding acquisition.

Funding: This research has been supported by the NSF I/UCRC for Embedded Systems at SIUC, and funded in part by the National Science Foundation (NSF) under Grant No. 0856039 and the UK Engineering and Physical Sciences Research Council (EPSRC) grant EP/F01869X. Any opinions, findings, and conclusions or recommendations expressed in this material are those of the authors and do not necessarily reflect the views of the NSF or EPSRC.

Acknowledgments: In this section you can acknowledge any support given which is not covered by the author contribution or funding sections. This may include administrative and technical support, or donations in kind (e.g., materials used for experiments).

Conflicts of Interest: The authors declare no conflict of interest. The funders had no role in the design of the study; in the collection, analyses, or interpretation of data; in the writing of the manuscript, or in the decision to publish the results.

References

1. Boeing Commercial Airplanes, “Statistical Summary of Commercial Jet Airplane Accidents Worldwide Operations - 1959–2015,” Jul. 2016.
2. T Yang, G Li, J Li, Y Zhang, X Zhang, Z Zhang, Z Li, “A Ground-Based Near Infrared Camera Array System for UAV Auto-Landing in GPS-Denied Environment”, Sensors 16, 1393, 20pp, 2016
3. P H Nguyen, K W Kim, Y W Lee, K R Park, “Remote Marker-Based Tracking for UAV Landing Using Visible-Light Camera Sensor. Sensors 17, 1987, 2017
4. G. Bhatnagar, Q. M. J. Wu, and Z. Liu, “Directive Contrast Based Multimodal Medical Image Fusion in NSCT Domain,” IEEE Trans. Multimed., vol. 15, no. 5, pp. 1014–1024, Aug. 2013.
5. R. Shen, I. Cheng, and A. Basu, “Cross-Scale Coefficient Selection for Volumetric Medical Image Fusion,” IEEE Trans. Biomed. Eng., vol. 60, no. 4, pp. 1069–1079, Apr. 2013.
6. F. Nencini, A. Garzelli, S. Baronti, and L. Alparone, “Remote Sensing Image Fusion Using the Curvelet Transform,” Inf. Fusion, vol. 8, no. 2, pp. 143–156, Apr. 2007.
7. S. Li, H. Yin, and L. Fang, “Remote Sensing Image Fusion via Sparse Representations Over Learned Dictionaries,” IEEE Trans. Geosci. Remote Sens., vol. 51, no. 9, pp. 4779–4789, Sep. 2013.
8. Zi Yang, Lilian S.C. Pun-Cheng, “Vehicle detection in intelligent transportation systems and its applications under varying environments: A review”, Image and Vision Computing, 2017, doi: /10.1016/j.imavis.2017.09.008
9. J Giralt, J Moreno-Garcia, L Jimenez-Linares, L Rodriguez-Benitez "A Road Departure Warning System Based on Video Motion Analysis and Fuzzy Logic", International Journal of Intelligent Systems, 32, 830-842, 2017.
10. S. Li and B. Yang, “A New Pan-Sharpening Method Using a Compressed Sensing Technique,” IEEE Trans. Geosci. Remote Sens., vol. 49, no. 2, pp. 738–746, Feb. 2011.
11. G Cai, P Jodoin, S ZiLi,Y D Wu, S Z Su, Z K Huang, "Perspective-SIFT: An efficient tool for low-altitude remote sensing image registration", Signal Processing, 93,(2013), 3088–3110
12. X. Qian, Y. Wang, and B. Wang, “Fast Color Contrast Enhancement Method for Color Night Vision,” Infrared Phys. Technol., vol. 55, no. 1, pp. 122–129, Jan. 2012.

13. H Li, H Qiu, Z Yu, B Li, "Multifocus image fusion via fixed window technique of multiscale images and non-local means filtering", Signal Processing, 138 (2017), 71-85
14. X Fu, D Zeng, Y Huang, Y Liao, X Ding, J Paisley, "A fusion-based enhancing method for weakly illuminated images", Signal Processing, 129 (2016) 82–96
15. Hui Xie; Kin Huat Low; Zhen He "Adaptive Visual Servoing of Unmanned Aerial Vehicles in GPS-denied Environments", IEEE/ASME Transactions on Mechatronics, in press (online) http://ieeexplore.ieee.org/stamp/stamp.jsp?tp=&arnumber=8048548, 10pp, 2017
16. M. Ding, L. Wei, and B. Wang, "Research on Fusion Method for Infrared and Visible Images via Compressive Sensing," Infrared Phys. Technol., vol. 57, pp. 56–67, Mar. 2013.
17. J. Shang and Z. Shi, "Vision-Based Runway Recognition for UAV Autonomous Landing," Int. J. Comput. Sci. Netw. Secur., vol. 7, no. 3, pp. 112–117, 2007.
18. A. Miller, M. Shah, and D. Harper, "Landing a UAV on a Runway Using Image Registration," in 2008 IEEE International Conference on Robotics and Automation, 2008, pp. 182–187.
19. L. G. Delphina and V. P. S. Naidu, "Detection of Airport Runway Edges Using Line Detection Techniques," 2011.
20. J. W. Han and L. Guo, "An Algorithm for Automatic Detection of Runways in Aerial Images," Mach. Graph. Vis. Int. J., vol. 10, no. 4, pp. 503–518, Sep. 2001.
21. Ö. Aytekin, U. Zöngür, and U. Halici, "Texture-Based Airport Runway Detection," IEEE Geosci. Remote Sens. Lett., vol. 10, no. 3, pp. 471–475, May 2013.
22. X. Wang, B. Li, and Q. Geng, "Runway Detection and Tracking for Unmanned Aerial Vehicle Based on an Improved Canny Edge Detection Algorithm," in 2012 4th International Conference on Intelligent Human-Machine Systems and Cybernetics, 2012, vol. 2, pp. 149–152
23. S. Cao, J. Jiang, G. Zhang, and Y. Yuan, "Runway Detection Using Line Segment Statistical model," in 2012 Third International Conference on Intelligent Control and Information Processing, 2012, pp. 601–604.
24. A. K. Tripathi and S. Swarup, "Shape and Color Features Based Airport Runway Detection," in 2013 3rd IEEE International Advance Computing Conference (IACC), 2013, pp. 836–841.
25. P. Gupta and A. Agrawal, "Airport Detection in High-Resolution Panchromatic Satellite Images," J. Inst. Eng. India, vol. 88, no. 5, pp. 3–9, 2007.
26. S. Sull and B. Sridhar, "Runway Obstacle Detection by Controlled Spatiotemporal Image Flow Disparity," IEEE Trans. Robot. Autom., vol. 15, no. 3, pp. 537–547, Jun. 1999.
27. C.-H. Pai, Y.-P. Lin, G. G. Medioni, and R. R. Hamza, "Moving Object Detection on a Runway Prior to Landing Using an Onboard Infrared Camera," in 2007 IEEE Conference on Computer Vision and Pattern Recognition, 2007, pp. 1–8.
28. R. Hamza, M. M. Ibrahim, D. Ramegowda, and V. Rao, "Runway Positioning and Moving Object Detection Prior to Landing," in Augmented Vision Perception in Infrared, London: Springer London, 2009.
29. C. Liu, Y. Zhang, K. Tan, and H. Yang, "Sensor Fusion Method for Horizon Detection From an Aircraft in Low Visibility Conditions," IEEE Trans. Instrum. Meas., vol. 63, no. 3, pp. 620–627, Mar. 2014.
30. Y.-F. Shen, Z.-U. Rahman, D. Krusienski, and J. Li, "A Vision-Based Automatic Safe Landing-Site Detection System," IEEE Trans. Aerosp. Electron. Syst., vol. 49, no. 1, pp. 294–311, Jan. 2013.
31. Y. Liu and F. Yu, "An Automatic Image Fusion Algorithm for Unregistered Multiply Multi-Focus Images," Opt. Commun., vol. 341, pp. 101–113, Apr. 2015.
32. P. Cheng, X. Li, Y. Wu, and S. Feng, "A Fusion of Real and Virtual Information for Aiding Aircraft Pilotage in Low Visibility," J. Comput., vol. 8, no. 4, Apr. 2013.
33. N. S. Kumar, S. K. Kashyap, V. P. S. Naidu, and G. Gopalratnam, "Integrated Enhanced and Synthetic Vision System for Transport Aircraft," Def. Sci. J., vol. 63, no. 2, pp. 157–163, Mar. 2013.
34. A Wong, P Fieguth, "Fast phase-based registration of multimodal image data", Signal Processing, 89, 2009, 724–737
35. B. Zitová and J. Flusser, "Image Registration Methods: A Survey," Image Vis. Comput., vol. 21, no. 11, pp. 977–1000, Oct. 2003.
36. R. C. Gonzalez and R. E. Woods, Digital Image Processing, 3rd edition. Upper Saddle River, N.J: Pearson, 2007.
37. S. Nikolov, P. Hill, D. Bull, and N. Canagarajah, "Wavelets for Image Fusion," in Wavelets in Signal and Image Analysis, Springer, 2001, pp. 213–241.

 doi:10.20944/preprints201810.0343.v1

38. S. Li and B. Yang, "Multifocus Image Fusion Using Region Segmentation and Spatial Frequency," Image Vis. Comput., vol. 26, no. 7, pp. 971–979, Jul. 2008.
39. W. F. J. Herrington, B. K. P. Horn, and I. Masaki, "Application of the Discrete Haar Wavelet Transform to Image Fusion for Nighttime Driving," in IEEE Proceedings. Intelligent Vehicles Symposium, 2005., 2005, pp. 273–277.
40. K. Rani and R. Sharma, "Study of Different Image Fusion Algorithms," Int. J. Emerg. Technol. Adv. Eng., vol. 3, no. 5, pp. 288–91, 2013.
41. D.-C. Tseng, Y.-L. Chen, and M. S. C. Liu, "Wavelet-Based Multispectral Image Fusion," in IGARSS 2001. Scanning the Present and Resolving the Future. Proceedings. IEEE 2001, 2001, vol. 4, pp. 1956–1958 vol.4.
42. H. Zheng, D. Zheng, Y. Sheng, and S. Li, "Study on the Optimal Parameters of Image Fusion based on Wavelet Transform," J. Comput. Inf. Syst., vol. 6, no. 1, pp. 131–137, 2010.
43. S. M. M. Rahman, M. O. Ahmad, and M. N. S. Swamy, "Contrast-Based Fusion of Noisy Images Using Discrete Wavelet Transform," IET Image Process., vol. 4, no. 5, pp. 374–384, Oct. 2010.
44. J. Núñez, X. Otazu, O. Fors, A. Prades, V. Palà, and R. Arbiol, "Multiresolution-Based Image Fusion with Additive Wavelet Decomposition," IEEE Trans. Geosci. Remote Sens., vol. 37, no. 3, pp. 1204–1211, May 1999.